Effect of ellipticity on Hanle electromagnetically induced absorption and transparency resonances with longitudinal and transverse magnetic fields

Nibedita Ram, M. Pattabiraman,[*] and C. Vijayan

Department of Physics, Indian Institute of Technology, Madras, Chennai 600036, India

The effect of incident light field ellipticity on the electromagnetically induced absorption (EIA) and electromagnetically induced transparency (EIT) resonances has been studied experimentally and computationally in Hanle configuration with longitudinal and transverse magnetic fields. We identify the Zeeman coherences that influence the resonance profile and study the role of coherence-transfer from excited to ground state via spontaneous emission as a function of ellipticity for the $F_g = 2 \rightarrow F_e = 3$ transition of ^{87}Rb. The EIT resonance observed with the light field locked on the $F_g = 1 \rightarrow F_e = 2$ transition of ^{87}Rb is an influence of the nearby $F_g = 1 \rightarrow F_e = 0$ closed and $F_g = 1 \rightarrow F_e = 1$ open transitions. With increase in ellipticity the observed EIA and EIT resonances diminish in amplitude for a longitudinal magnetic field and are enhanced for a transverse magnetic field. We computationally account for these observations and discuss the factors that influence the EIA and EIT resonance amplitudes as a function of ellipticity and show that for a transverse field scan the ellipticity dependence of the EIA resonance amplitude can be accounted for without invoking the Doppler effect unlike for a longitudinal field scan. We also show that the maximum in the EIA resonance amplitude obtained for nonzero ellipticities with a longitudinal magnetic field depends on the closedness of the atomic system.

I. INTRODUCTION

The interaction of atoms with coherent light fields results in interesting phenomena such as electromagnetically induced transparency (EIT), electromagnetically induced absorption (EIA), coherent population trapping (CPT), and lasing without inversion (LWI) [1–4]. This coherent interaction leads to interesting applications such as slow light, atomic clocks, and sensitive magnetometry [5–7]. An atomic system with a degenerate ground state subject to a resonant pump field and a tuneable probe field exhibits a sharp decrease in probe absorption, referred to as EIT, when the probe and pump frequencies are the same. EIT can be interpreted as atoms being pumped into a so-called dark state (due to a superposition of the ground states) which is not coupled to the excited state [1]. EIA refers to the significant enhancement of the absorption of a probe field in degenerate two-level systems subject to a pump field [2]. EIA can be explained in terms of transfer of coherence (TOC) between the excited and ground states via spontaneous emission [8–10]. EIT and EIA in degenerate two level systems can be observed in two configurations: either by detuning one optical field with respect to the other or by using one resonant optical field and measuring the transmission or fluorescence as a function of a magnetic field scanned through zero referred to as the Hanle configuration [11].

The ellipticity of the coherent probe beam was found to have a significant influence on the Hanle EIA signal. Brazhnikov *et al.* found that the EIA resonance amplitude peaks at a nonzero value of ellipticity (ε). They could reproduce their data only when the influence of Doppler broadening was taken into account [12]. In contrast the EIT resonance amplitude is maximum for linear polarization ($\varepsilon = 0$). Dimitrijević *et al.* observed a shift in the EIA resonance amplitude peak to higher ellipticities with increase in light intensity which they

attributed to an intimate interplay among optical pumping, ellipticity, and atomic velocity [13–15]. These studies were performed with a magnetic field parallel (longitudinal) to the direction of light propagation. Hanle EIA profiles obtained with a transverse magnetic field are also of interest. EIA resonances with circularly polarized light with a transverse magnetic field were found to be more pronounced than those obtained with linearly polarized light [16].

In this report we experimentally and computationally study the influence of ellipticity on the TOC process by studying Hanle EIA profiles of a closed transition, $F_g = 2 \rightarrow F_e = 3$ of ^{87}Rb, with a longitudinal and transverse magnetic fields. We identify the Zeeman coherences responsible for the EIA resonance as a function of light ellipticity and show that for Hanle profiles with a transverse magnetic field, Doppler broadening need not be considered to study the influence of light ellipticity. We compare these results with the Hanle profiles obtained with longitudinal and transverse magnetic fields when the probe beam is locked to the $F_g = 1 \rightarrow F_e = 2$ transition of ^{87}Rb. Although an EIA resonance is expected, being a $F_g \rightarrow F_{g+1}$ transition, an EIT resonance was observed due to the strong influence of the nearby $F_g = 1 \rightarrow F_e = 0$ (closed system) and $F_g = 1 \rightarrow F_e = 1$ (open system) transitions. We computationally study the factors that influence the EIA and EIT resonance amplitudes as a function of ellipticity and show that the EIA amplitude maximum obtained for nonzero ellipticities with a longitudinal magnetic field depends on the closedness of the atomic system.

II. EXPERIMENTAL DESCRIPTION

The experimental setup used for measurement of EIA in Hanle configuration is shown in Fig. 1. An external cavity diode laser of wavelength 780 nm is locked to the hyperfine transitions, $F_g = 2 \rightarrow F_e = 3$ or $F_g = 1 \rightarrow F_e = 2$ of ^{87}Rb (Fig. 2) using a saturation absorption spectroscopy set up
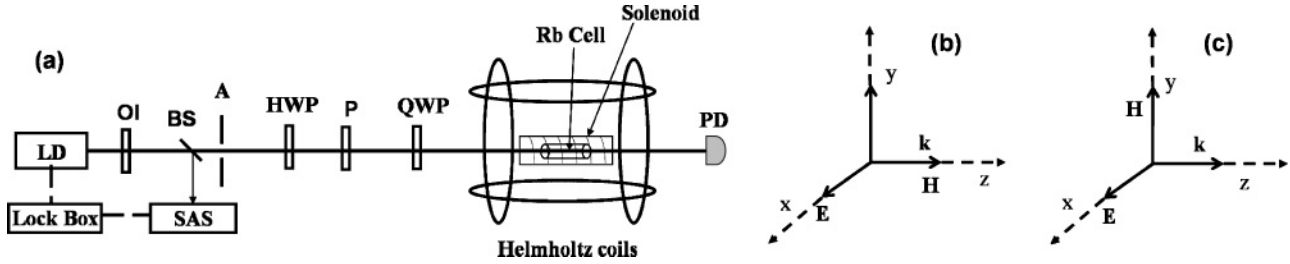
---

*pattu@physics.iitm.ac.in

FIG. 1. Schematic of the experimental arrangement used. Key: LD, laser diode; OI, optical isolator; BS, beam splitter; A, aperture; HWP, half waveplate; P, polarizer; QWP, quarter waveplate; PD, photo detector; SAS, saturation absorption spectroscopy setup. Longitudinal (b) and transverse (c) field scan configurations showing the directions of the magnetic field (**H**), probe field propagation (k), and light polarization (E).

by dither-lock technique with a reference signal of 800 Hz. A glass cell of length 10 cm containing a natural mixture of two isotopes of rubidium (^{85}Rb, 72%, and ^{87}Rb, 28%) is placed inside a solenoid and is surrounded by two pairs of coils in Helmholtz configuration. Signals are obtained by varying the magnetic field along the z axis (longitudinal field scan) or y axis (transverse field scan) through zero. For both cases the magnetic fields in the two other orthogonal directions were reduced below 10 mG. The intensity of the beam used in the experiment was controlled by using a half waveplate and polarizer. A quarter waveplate was used to change the ellipticity of the beam. The diameter of probe beam used was 4.5 mm. The probe beam transmission was measured with a photo detector interfaced with a computer.

Hanle transmission profiles obtained for the transitions $F_g = 2 \rightarrow F_e = 3$ and $F_g = 1 \rightarrow F_e = 2$ with longitudinal and transverse magnetic field scans are shown in Figs. 3 and 4 respectively for different ellipticities. For linearly polarized light, the $F_g = 2 \rightarrow F_e = 3$ transition exhibits an EIA resonance as expected [9]. The $F_g = 1 \rightarrow F_e = 2$ transition exhibits an EIT resonance as against the expected EIA resonance for a $F_g \rightarrow F_{g+1}$ transition. Similar dark resonances in $F_g \rightarrow F_{g+1}$ transitions were recently observed by Andreeva *et al.* on the D_2 transition of Cesium using an extremely thin cell [17] and by Auzinsh *et al.* [18] in $F_g = 2 \rightarrow F_e = 3$, D_1 transition of ^{85}Rb. Auzinsh *et al.* [18] attributed this to the strong influence of the dark resonance (EIT) exhibited by the neighboring $F_g = 2 \rightarrow F_e = 2$ transition which lies

361.6 MHz lower. They were able to detect a weak bright resonance (EIA) when the probe laser was detuned 240 MHz from the $F_g = 2 \rightarrow F_e = 3$ transition.

The EIT observed by us at the $F_g = 1 \rightarrow F_e = 2$ (D_2) transition of ^{87}Rb (Fig. 2) may also originate due to a similar reason: in this case the likely dominant influence being the dark resonance associated with the neighboring $F_g = 1 \rightarrow F_e = 0$ and $F_g = 1 \rightarrow F_e = 1$ transitions (Fig. 2). In support of this idea, we note that Zibrov and Masko [19] observed a Hanle bright resonance on the Doppler broadened $F_g = 1 \rightarrow F_e = 0, 1, 2$ (D_2; ^{87}Rb) transition only when the probe beam is detuned to the high-frequency side of the Doppler profile. A dark resonance is observed at the center of the Doppler profile due to the interaction with the $F_g = 1 \rightarrow F_e = 0$ transition. The $F_g = 1 \rightarrow F_e = 2$ (D_2; ^{87}Rb) transition suffers a 50% population loss to the other ground-state hyperfine sublevel ($F_g = 2$) [20]. This results in a significant decrease in transfer of coherence to $F_g = 1$ resulting in a weak bright resonance susceptible to the influence of the stronger dark resonances. Hanle profiles obtained by red shifting the laser frequency from
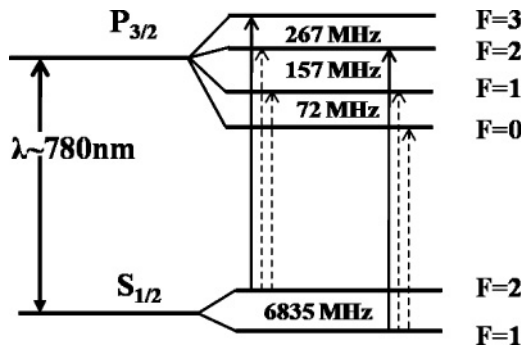

FIG. 2. Energy level diagram for ^{87}Rb. The selection rule for optical transitions (up arrows) is $\Delta F = 0, \pm1$. The transitions experimentally accessed are shown by solid up arrows.
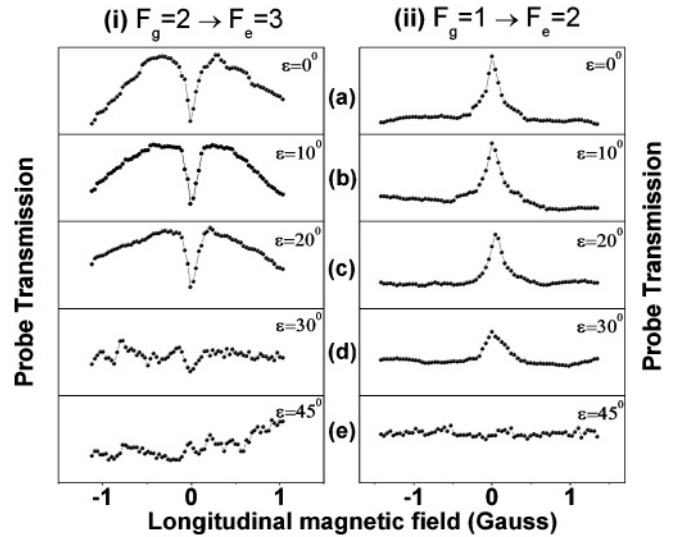

FIG. 3. Probe transmission plotted as a function of longitudinal magnetic field for (i) $F_g = 2 \rightarrow F_e = 3$ (probe intensity of 446 μW/cm^2) and (ii) $F_g = 1 \rightarrow F_e = 2$ (probe intensity of 1.258 mW/cm^2) with ellipticity (a) $\varepsilon = 0°$, (b) $10°$, (c) $20°$, (d) $30°$, (e) $45°$. All plots have been vertically shifted and have been plotted with the same y axis scale as that of (a) for comparison.
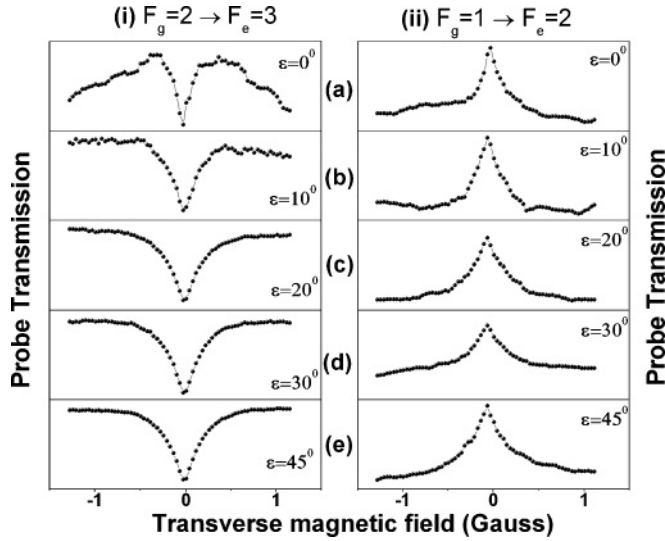
FIG. 4. Probe transmission plotted as a function of transverse magnetic field for (i) $F_g = 2 \rightarrow F_e = 3$ (probe intensity of 446 μW/cm^2) and (ii) $F_g = 1 \rightarrow F_e = 2$ (probe intensity of 1.258 mW/cm^2) with ellipticity (a) $\varepsilon = 0°$, (b) $10°$, (c) $20°$, (d) $30°$, (e) $45°$.

$F_g = 1 \rightarrow F_e = 2$ toward the $F_g = 1 \rightarrow F_e = 0, 1$ transitions up to 160 MHz using an acousto-optic modulator resulted in more pronounced EIT profiles (not shown). On the other hand, blue shifting rapidly weakens the EIT and results in a noisy Hanle profile. Though we could not obtain an EIA profile for blue shifts up to 160 MHz (not shown) the observed trend supports the dominant influence of the $F_g = 1 \rightarrow F_e = 0$ and $F_g = 1 \rightarrow F_e = 1$ transitions.

The amplitudes of the bright (EIA) resonance observed on $F_g = 2 \rightarrow F_e = 3$ and the dark resonance observed on $F_g = 1 \rightarrow F_e = 2$ diminish with increase in light ellipticity in a longitudinal field scan vanishing for circularly polarized light (Fig. 3). In contrast both resonances grow more prominent with ellipticity in a transverse field scan (Fig. 4). This behavior is clearly seen in Figs. 5 and 6 where the amplitudes of the bright and dark resonances are plotted as a function of light

ellipticity for longitudinal and transverse magnetic field scans respectively. For $F_g = 2 \rightarrow F_e = 3$, a prominent peak in the EIA amplitude is observed with increase in laser power around $\varepsilon \sim 10$-$20°$ with a longitudinal magnetic field ([Fig. 5(a)]. The peak shifts to higher ellipticities with increase in laser power. These observations are in agreement with previous reports for longitudinal magnetic fields [13,14]. The bright resonance amplitude for $F_g = 2 \rightarrow F_e = 3$ obtained with a transverse field [Fig. 6(a)] increases with ellipticity and is highest for circularly polarized light ($\varepsilon = 45°$) in agreement with [16]. The dark resonance amplitude obtained with a longitudinal field scan does not exhibit a peak [Fig. 5(b)]. For a transverse field scan the dark resonance amplitude increases steeply for $\varepsilon < 20°$ and exhibits a much slower increase at higher ellipticities [Fig. 6(b)]. In order to explain these results we have performed a density matrix based computation discussed in the next section.

III. THEORETICAL MODEL

The Hanle bright resonance profiles were computed by solving optical Bloch equations for a $F_g = 1 \rightarrow F_e = 2$ transition for different optical field ellipticities. This transition was chosen for computation since it is the simplest $F_g \rightarrow F_{g+1}$ transition which gives rise to an EIA resonance. We chose a closed $F_g = 1 \rightarrow F_e = 0$ system as a model transition to understand the dark resonance data. The level configurations and allowed transitions for both computational systems are shown in Fig. 7: the ground-state and excited-state Zeeman sublevels are represented by g_i and e_i respectively. The quantization axis was chosen parallel to the direction of magnetic field along the z axis. For longitudinal field scans the probe propagation direction was taken along the z axis and its electric field vector was taken along the x axis. For transverse field scans the probe propagation direction was taken along the y axis with its electric field vector along the x axis. For $\varepsilon = 0$, the probe field then becomes σ polarized (selection rule: $\Delta m = \pm 1$) for both scan configurations. In a longitudinal field scan change in ellipticity results in an unequal mixture of σ^+ and σ^- polarizations. In a transverse field scan nonzero ellipticities result in π transitions (selection rule: $\Delta m = 0$).
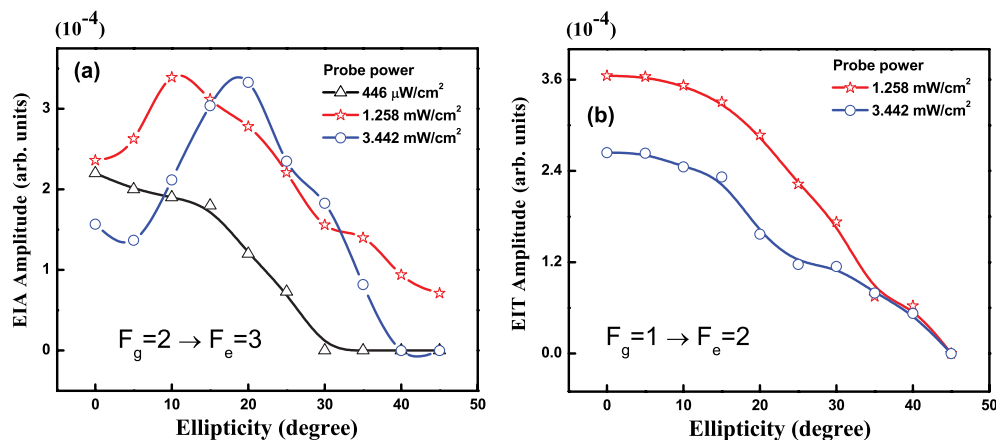

FIG. 5. (Color online) EIA and EIT amplitudes with a longitudinal field scan plotted as a function of ellipticity for (a) $F_g = 2 \rightarrow F_e = 3$ and (b) $F_g = 1 \rightarrow F_e = 2$. The solid lines guide the eye. The probe intensities used are indicated in the plots.
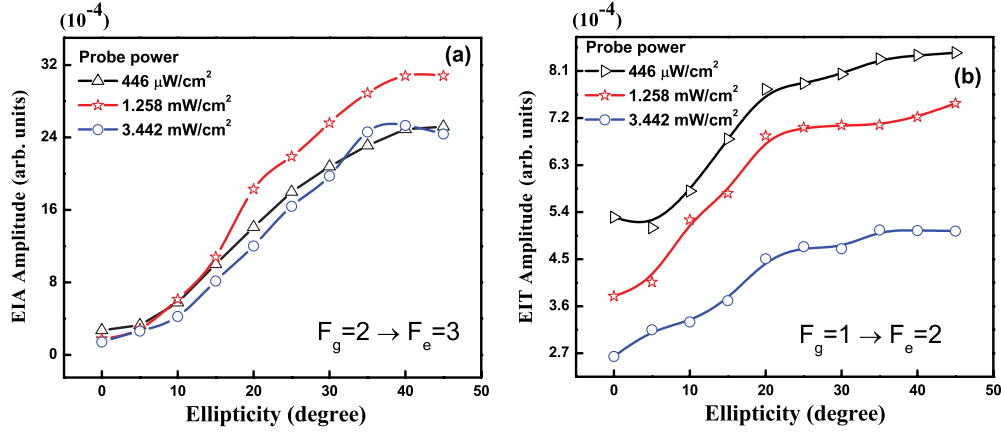
FIG. 6. (Color online) EIA and EIT amplitudes with a transverse field scan plotted as a function of ellipticity for (a) $F_g = 2 \rightarrow F_e = 3$ and (b) $F_g = 1 \rightarrow F_e = 2$. The solid lines guide the eye. The probe intensities used are indicated in the plots.

The electric field vector $\mathbf{E} = E_0 \hat{e} e^{-i\omega t} + $ c.c. is the electric field, ω is the frequency of the probe beam, and $\hat{e}$ its unit polarization vector given by

$$\hat{e} = \hat{e}_x \cos \varepsilon + i \hat{e}_y \sin \varepsilon$$

$$= -\hat{e}_{+1} \cos(\varepsilon - \pi/4) - \hat{e}_{-1} \sin(\varepsilon - \pi/4).$$

Where $\hat{e}_{\pm} = \mp(\hat{e}_x + \hat{e}_y)/\sqrt{2}$ cyclic basis vectors and $\varepsilon = -\frac{\pi}{4} \leqslant \varepsilon \leqslant \frac{\pi}{4}$ the ellipticity of the probe field.

The total Hamiltonian H is the sum of the unperturbed Hamiltonian H_0, the light-atom interaction Hamiltonian H_1, and the magnetic-field atom interaction Hamiltonian H_B, with

$$H_0 = \sum_i \hbar \omega_{g_i} |g_i\rangle \langle g_i| + \sum_i \hbar \omega_{e_i} |e_i\rangle \langle e_i| \qquad (1)$$

$$H_1 = \sum_{e_j, g_k} |e_j\rangle \langle g_k| \left[i\mathbf{E}.\mathbf{d}_{e_j g_k} \right] + \text{H.c.}, \qquad (2)$$

where H.c. is the Hermitian conjugate of first term of (2). The dipole matrix element $\mathbf{d}_{e_j g_k}$ is given by

$$\mathbf{d}_{e_j g_k} = \langle F_e \| e\mathbf{r} \| F_g \rangle (-1)^{F_e - 1 + m_g}$$

$$\times \begin{pmatrix} F_e & 1 & F_g \\ -m_e & q & m_g \end{pmatrix}; \quad \tilde{q} = 0, \pm 1.$$

The parentheses denotes the $3j$ symbol.

$$H_B = \sum_{i \neq 0} g \mu_B \mathbf{H} \{ m_{g_i} |g_i\rangle \langle g_i| + m_{e_i} |e_i\rangle \langle e_i| \}. \qquad (3)$$

Where $\mathbf{H}$ is the applied magnetic field, the Bohr magneton (1.399 MHz/gauss) and g the gyromagnetic ratio. In the computation we express the magnetic field in terms of the Larmor frequency, $\hbar \omega_L = g \mu_B \mathbf{H}$. The Rabi frequency associated with individual probe transitions is given by,

$$\Omega_{e_j g_k} = E_0 d_{e_j g_k}/\hbar = (-1)^{F_e - 1 + m_g} \begin{pmatrix} F_e & 1 & F_g \\ -m_e & q & m_g \end{pmatrix} \Omega,$$

where $\Omega = \langle F_e \| e\mathbf{r} \| F_g \rangle E_0/\hbar$ is the general Rabi frequency of the $F_g \rightarrow F_e$ transition.

Substituting $\Omega_{e_j g_k}$ in (2) we get

$$H_1 = \hbar \sum_{e_j, g_k} |e_j\rangle \langle g_k| \left[\Omega_{e_j g_k} e^{-i\omega t} \right].\hat{\mathbf{V}} + \text{H.c.}$$

The operator $\hat{\mathbf{V}}$ is expressed in terms of the Clebsch-Gordan (CG) coefficients as

$$\hat{\mathbf{V}} = \sum_{q=\pm 1, m_e, m_g} \text{CG}^{F_e, m_e}_{F_g, m_g; 1, q} e^q |F_e, m_e\rangle \langle F_g, m_g|,$$

where $e^{+1} = -\cos(\varepsilon - \pi/4)$ and $e^{-1} = -\sin(\varepsilon - \pi/4)$ are component of unit complex elliptic polarization vector in cyclic basis [12].
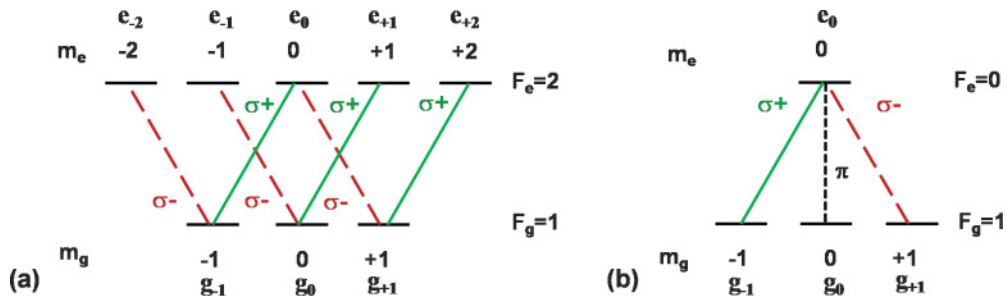

FIG. 7. (Color online) Atomic level configuration for the transitions (a) $F_g = 1 \rightarrow F_e = 2$ and (b) $F_g = 1 \rightarrow F_e = 0$ used in the computation.

The total Hamiltonian after the application of the rotating wave approximation, $\bar{H}$, is used in the Liouville equation [21] which gives the evolution of the density matrix ρ

$$\frac{d\rho}{dt} = \frac{1}{i\hbar}[\bar{H}, \rho] - \frac{1}{2}\{R, \rho\} + \Lambda_\Gamma + \Lambda\gamma. \quad (4)$$

The square brackets and the curly brackets denote the commutator and anticommutator respectively. R is a diagonal matrix which represents the spontaneous decay of the excited state at a rate Γ and the ground-state collisional decay rate γ_g. An additional excited state collisional decay rate $\gamma_e = (\gamma_g = \gamma)$ is also included. Off-diagonal collisional dephasing terms are not included. The matrices Λ_Γ and $\Lambda\gamma$ represent the repopulation of the ground state due to the relaxation terms Γ and γ respectively. The right-hand side of (4) can be set to zero and the 64 optical Bloch equations can be numerically solved in the steady-state approximation as a set of coupled linear algebraic equations [22]. The Hanle absorption signal in the presence of a longitudinal field is given by

$$\alpha = \sum_{e_j, g_k} \frac{2\sqrt{2}\pi\omega_0 N}{\hbar c \Omega} |\mathbf{d}_{e_j g_k}|^2 (\cos\varepsilon + \sin\varepsilon) \text{Im}[\rho_{e_j g_k}]. \quad (5)$$

The Doppler effect was taken into account by averaging absorption profiles calculated for single atomic velocities with varying weights obtained from the Maxwell-Boltzmann distribution [15].

In order to examine how the Hanle signal depends on the TOC among different excited and ground-state coherences, the repopulation matrix Λ_Γ was rewritten in such a way that specific TOC channels from excited state coherences can be set to zero in the computation [23]. The total repopulation is expressed as 8×8 matrix of the form

$$\Lambda_\Gamma = \begin{pmatrix} A & B \\ C & D \end{pmatrix}.$$

Here A is a matrix in which the diagonal elements involve excited state population and the off-diagonal elements involve excited state coherences. The other submatrices B, C, and D are null matrices. The matrix A is given by

$$A = \begin{pmatrix} \Lambda_\Gamma(1,1) & \Lambda_\Gamma(0,1) & \Lambda_\Gamma(-1,1) \\ \Lambda_\Gamma(1,0) & \Lambda_\Gamma(0,0) & \Lambda_\Gamma(-1,0) \\ \Lambda_\Gamma(1,-1) & \Lambda_\Gamma(0,-1) & \Lambda_\Gamma(-1,-1) \end{pmatrix}.$$

A few diagonal (6) and off diagonal [(7) and (8)] elements of A are given below.

$$\Lambda_\Gamma(1,1) = b_0 \Gamma \sum_{n=0}^{2} \left[CG_{F_g m_{g_{n-2}}, F_g m_{g_2}}^{F_e m_{e_n}} \right]^2 \rho_{e_n e_n} \quad (6)$$

$$\Lambda_\Gamma(0,1) = b_1 \Gamma \sum_{n=0}^{2} \left[CG_{F_g m_{g_{n-1}}, F_g m_{g_2}}^{F_e m_{e_{n+1}}} \right] \left[CG_{F_g m_{g_{n-1}}, F_g m_{g_1}}^{F_e m_{e_n}} \right] \rho_{e_n e_{n-1}} \quad (7)$$

$$\Lambda_\Gamma(-1,1) = b_2 \Gamma \sum_{n=-1}^{+1} \left[CG_{F_g m_{g_n}, F_g m_{g_2}}^{F_e m_{e_n}} \right] \left[CG_{F_g m_{g_n}, F_g m_{g_0}}^{F_e m_{e_{n+1}}} \right] \rho_{e_n e_{n-2}}, \quad (8)$$

where $[CG_{F_g m_{g_{n-1}}, F_g m_{g_2}}^{F_e m_{e_{n+1}}}]$, etc., are the Clebsch Gordan (CG) coefficients for the levels involved in the transition.

The diagonal terms of A are multiplied by a constant b_0 and the off-diagonal terms of A involving the excited state coherences, $\Delta m_{ee} = \pm 1$, and ± 2, are multiplied by constants b_1 and b_2, respectively. Usually all these constants are equal and refer to the branching ratio of a transition. If all the constants are equal to 1, the transition becomes closed. Transfer of population is represented by b_0. If we set $b_2 = 0$ ($b_1 = 0$), the TOC involving $\Delta m_{ee} = \pm 2$ ($\Delta m_{ee} = \pm 1$) and $\Delta m_{gg} = \pm 2$ ($\Delta m_{gg} = \pm 1$) is eliminated from the computation. This allows us to explore the role of TOC when the ellipticity of the optical field is varied.

A. Computational results

1. Longitudinal field scan for $F_g = 1 \rightarrow F_e = 2$

The computed probe absorption for the $F_g = 1 \rightarrow F_e = 2$ closed transition with, $b_0 = 1$, for a longitudinal magnetic field is shown in Fig. 8 (column i) for different ellipticities. The computation was done with $\Gamma/\gamma = 1000$ and $\Omega/\Gamma = 0.2$. When the magnetic field is taken along the quantization axis, the observed EIA can be understood in terms of the creation of Zeeman coherences at zero magnetic field and their destruction at nonzero magnetic fields [24]. When the ellipticity of incident field increases the EIA amplitude decreases as shown in Fig. 8 [column i, panels (a)–(d)] ($b_2 = b_1 = 1$) in agreement with experiment. When the probe field becomes circularly polarized, the EIA resonance vanishes [Fig. 8, column i, panel (d)]. The steady-state optical Bloch equation for each probe transition
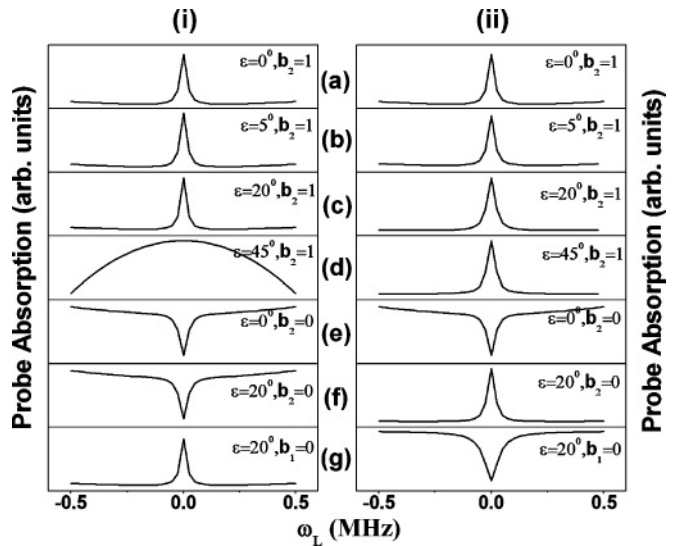

FIG. 8. Computed total probe absorption with longitudinal (i) and transverse (ii) field scans for $F_g = 1 \rightarrow F_e = 2$ with ellipticity, (a) $\varepsilon = 0°$, (b) $5°$, (c) $20°$, (d) $45°$. TOC from $\Delta m = \pm 2$ coherence is set to zero ($b_2 = 0$) in (e) and (f). TOC from $\Delta m = \pm 1$ coherence is set to zero ($b_1 = 0$) in (g). Other parameters used in the computation, $\Gamma/\gamma = 1000$ and $\Omega/\Gamma = 0.2$.
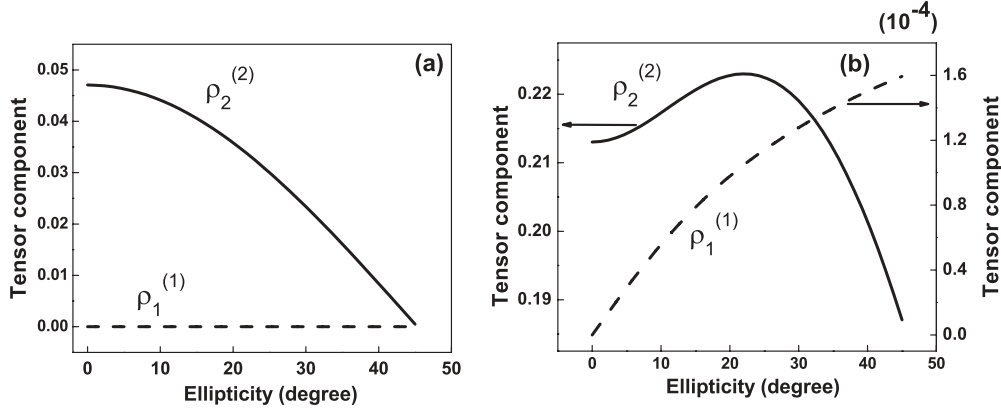
FIG. 9. Real part of excited state dipole, $\rho_1^{(1)}$, and quadrupole, $\rho_2^{(2)}$, tensor components versus ellipticity for a closed transition $F_g = 1 \rightarrow F_e = 2$ with a longitudinal (a) and transverse (b) magnetic field of $\omega_L/\Gamma = 0.0001$, $\Gamma/\gamma = 1000$, $\Omega/\Gamma = 0.2$, and $b_i = 1$.

[Fig. 7(a)] for a longitudinal field scan is given by

$$
\begin{aligned}
0 = &-\left(\gamma + \frac{\Gamma}{2}\right)\rho_{e_n g_{n+1}} \\
&-\frac{1}{4}i\Omega_{e_n g_{n+1}}[(3j)_{n+2,n+1}\{(1+i)e^{-i\varepsilon}+(1-i)e^{i\varepsilon}\}\rho_{e_n e_{n+2}} \\
&+(3j)_{n,n+1}\{(1-i)e^{-i\varepsilon}+(1+i)e^{i\varepsilon}\}(\rho_{g_{n+1}g_{n+1}}-\rho_{e_n e_n}) \\
&-(3j)_{n,n-1}\{(1+i)e^{-i\varepsilon}+(1-i)e^{i\varepsilon}\}\rho_{g_{n-1}g_{n+1}}] \\
&-i[n\omega_L+(-\Delta+\omega_L)\rho_{e_n g_{n+1}}]; \quad n = -2, -1, 0 \quad (9)
\end{aligned}
$$

It is seen that the optical coherences which contribute to the total absorption depend on next-near-neighbour coherences which connect Zeeman sublevels with $\Delta m = \pm 2$. When the absorption was computed by removing the TOC contribution from next-near-neighbor coherences, that is, by setting $b_2 = 0$, a dark resonance is observed as seen from Fig. 8 [column i, panel (e)] for $\varepsilon = 0°$ and Fig. 8 [column i, panel (f)] for $\varepsilon = 20°$. Thus the enhanced absorption Hanle signal is a direct consequence of TOC of $\Delta m = \pm 2$ coherences [25]. The EIA resonance profile is unchanged when the TOC contribution from $\Delta m = \pm 1$ coherences is removed ($b_1 = 0$) [Fig. 8, column i, panel (g)] as maybe expected in the absence of π transitions.

The Zeeman coherences can be expressed in terms of light induced multipole moments and these can be obtained in terms of the irreducible tensor representation of the density matrix [26]

$$
\rho = \sum_{k=0}^{2F} \sum_{Q=-k}^{+k} \rho_Q^{(k)} T_Q^{(k)}, \quad (10)
$$

where $T_Q^{(k)}$ are the irreducible tensor components and $\rho_Q^{(k)}$ are the state multipoles with $k = 0, 1, \ldots 2F$ and $Q = -k, \ldots, k$. The multipoles are related to the Zeeman coherences by

$$
\rho_Q^{(k)} = \sum_{m,m'=-F}^{F} (-1)^{F-m'} \langle F, m, F, -m' \| k, Q \rangle \rho_{m,m'}. \quad (11)
$$

The excited state quadrupole moment, $\rho_2^{(2)}$, and the excited state dipole moment, $\rho_1^{(1)}$, are given by the weighted sum of the $\Delta m_{ee} = \pm 2$ and $\Delta m_{ee} = \pm 1$ coherences respectively,

$$
\rho_2^{(2)} = (3j)_{n,n-2} \sum_{n=0}^{2} \rho_{e_n e_{n-2}} \quad (12)
$$

$$
\rho_1^{(1)} = (3j)_{n,n-1} \sum_{n=-1}^{2} \rho_{e_n e_{n-1}}. \quad (13)
$$

The real part of (12) and (13) plotted as a function of ellipticity for a longitudinal magnetic field, $\omega_L/\Gamma = 0.0001$ is shown in Fig. 9(a). The overall decrease in the magnitude of the excited state $\Delta m = \pm 2$ coherences with increase in ellipticity [Fig. 9(a)], suggests a corresponding decrease in TOC of $\Delta m = \pm 2$ coherences resulting in a decrease in the EIA resonance amplitude. However, this does not account for the peak observed in the EIA amplitude for nonzero ellipticities.
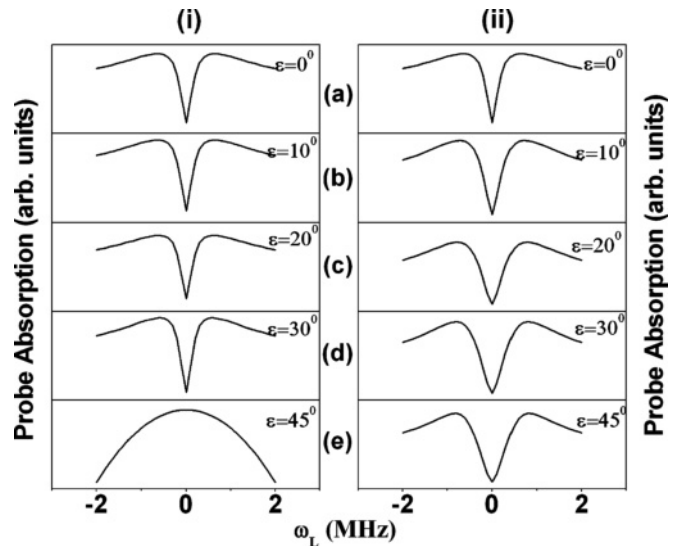

FIG. 10. Computed total probe absorption with longitudinal (i) and transverse (ii) field scans for the closed $F_g = 1 \rightarrow F_e = 0$ transition with ellipticity, (a) $\varepsilon = 0°$, (b) $10°$, (c) $20°$, (d) $30°$, (e) $45°$. Parameter used in computation: $\Gamma/\gamma = 1000$ and $\Omega/\Gamma = 0.2$.
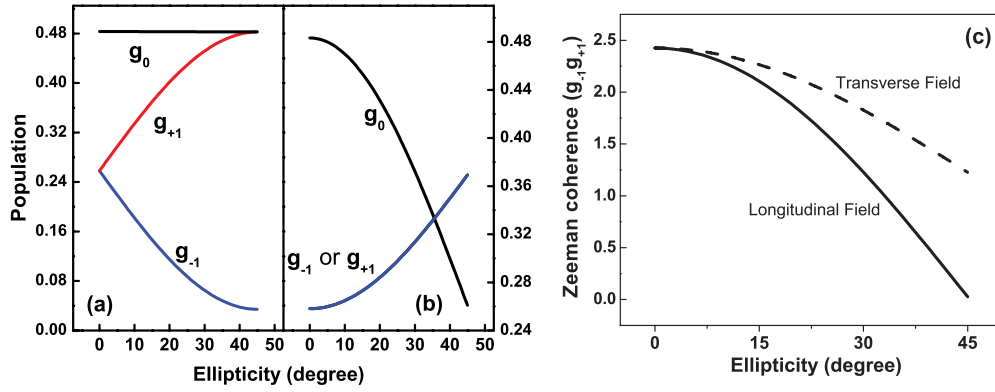
FIG. 11. (Color online) Population of the Zeeman sublevel of $F_g = 1$ as a function of light ellipticity for a (a) longitudinal field scan and (b) transverse field scan. (c) Real part of $g_{-1}g_{+1}$ (Zeeman coherence) as a function of light ellipticity for both field configurations. Parameters used $\omega_L = 0$, $\Gamma/\gamma = 1000$, and $\Omega/\Gamma = 0.2$. Although the magnetic field was set to zero, the observed behavior depends on the probe field propagation direction with respect to the axis of quantization.

This issue is taken up in detail below. For circularly polarized light, $\rho_2^{(2)} = 0$ and hence no EIA is possible [Fig. 8, column i, panel (d)]. Alternatively the absence of the EIA can be attributed to the accumulation of the population on the extreme ground-state Zeeman sublevel which cannot be redistributed by the magnetic field. The dipole moment, $\rho_1^{(1)} = 0$ for all ellipticities and hence $\Delta m = \pm 1$ coherences have no influence on the EIA profile for a longitudinal magnetic field.

2. Transverse field scan for $F_g = 1 \rightarrow F_e = 2$

The computed probe absorption for the $F_g = 1 \rightarrow F_e = 2$ transition ($b_0 = 1$), with a transverse magnetic field is shown in Fig. 8 (column ii) for different ellipticities. The computation was done with $\Gamma/\gamma = 1000$ and $\Omega/\Gamma = 0.2$. The EIA resonance amplitude grows prominent with increase in light ellipticity and is maximum for circularly polarized light [Fig. 8, column ii, panels (a)–(d)] in agreement with experiment. For linearly polarized light, a zero field dip is observed with $b_2 = 0$ [Fig. 8, column ii, panel (e)]. For $\varepsilon \neq 0$, the absence of TOC from $\Delta m = \pm 1$ coherences ($b_1 = 0$) also results in a zero field dip [Fig. 8, column ii, panel (g)]. The influence of b_2 decreases with increase in ε and for $\varepsilon \geqslant 20°$, setting $b_2 = 0$ only results in a slight decrease in the EIA peak amplitude. Thus TOC from both $\Delta m = \pm 2$ and $\Delta m = \pm 1$ coherences contribute to the enhancement of the EIA resonance amplitude observed with a transverse field scan due to presence of a π-polarized light field component for nonzero ellipticities. This can also be seen from the increase observed in the real parts of $\rho_1^{(1)} = 0$ with increase in ellipticity for a transverse magnetic field of $\omega_L/\Gamma = 0.0001$ [Fig. 9(b)]. Although $\Delta m = \pm 1$ coherences are about 100 times smaller than $\Delta m = \pm 2$ coherences they are more influential on the Hanle profile for nonzero ellipticities.

3. Longitudinal and transverse field scans for $F_g = 1 \rightarrow F_e = 0$

The computed probe absorption for the closed transition, $F_g = 1 \rightarrow F_e = 0$ [Fig. 7(b)] with longitudinal and transverse field scans is shown in columns (i) and (ii) of Fig. 10 respectively. The computation was performed with $\Gamma/\gamma = 1000$ and $\Omega/\Gamma = 0.2$. The EIT resonance amplitude decreases

for a longitudinal field scan and increases for a transverse field scan with increase in ellipticity in agreement with experiment. Since the excited state, $F_e = 0$, is nondegenerate, the repopulation matrix, Λ_Γ, appearing in (4) is diagonal and TOC does not occur. When the ellipticity of the probe field is varied for a longitudinal field scan, population from one of the extreme ground-state Zeeman sublevel (say g_{-1}) gets transferred to another (say g_{+1}) for $F_g = 1$. The population in g_0 remains nearly unchanged since it is not connected by an optical transition [Fig. 11(a)]. The resulting imbalance between σ^+ and σ^- polarization components weakens the dark state, $(|g_{+1}\rangle - |g_{-1}\rangle)/\sqrt{2}$, responsible for the EIT eventually destroying it for $\varepsilon = 45°$. This can also be inferred from the decrease in magnitude of the real part of the Zeeman coherence, $g_{-1}g_{+1}$, with ellipticity [Fig. 11(c)].

For a transverse magnetic field, with nonzero ellipticities there is no imbalance between σ^+ and σ^- polarization components but a π component is introduced. With increase
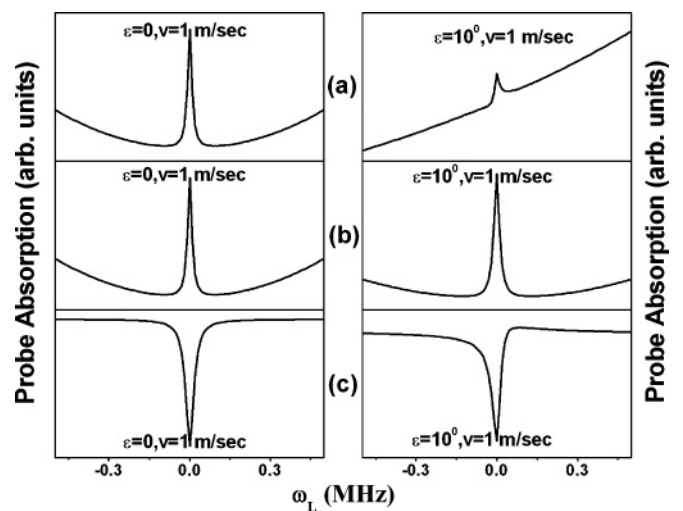

FIG. 12. Total probe absorption for $F_g = 1 \rightarrow F_e = 2$ with a (a) longitudinal and (b) transverse field scan and total probe absorption for $F_g = 1 \rightarrow F_e = 0$ with a (c) longitudinal field scan with $\varepsilon = 0°$ and $10°$ with different atomic velocities (detuning). Other parameters used: $\Gamma/\gamma = 1000$, $\Omega/\Gamma = 0.2$, and $b_i = 1$.
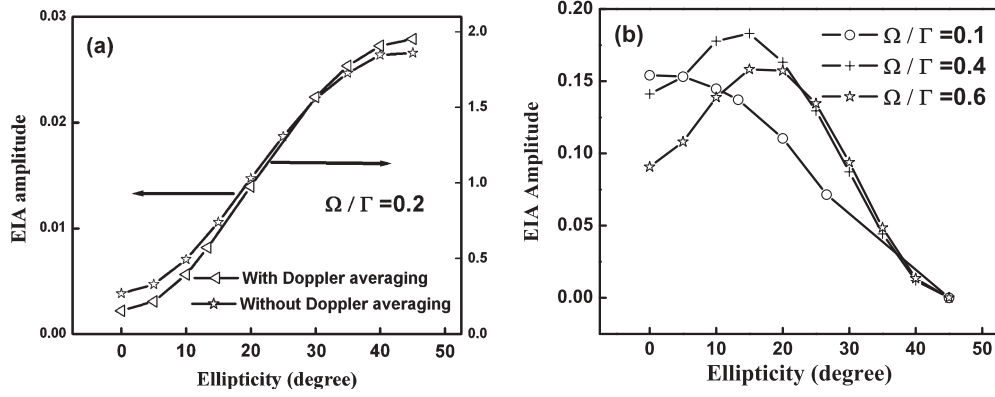
FIG. 13. (a) Computed EIA amplitude for $F_g = 1 \rightarrow F_e = 2$ with a transverse field scan with and without Doppler averaging. (b) Doppler averaged EIA amplitude for a longitudinal field scan. Parameters used: $\Gamma/\gamma = 1000$, $b_i = 1$. The Rabi frequencies used are indicated in the plots.

in ellipticity the π components transfer population from the g_0 sublevel equally to both g_{-1} and g_{+1} sublevels, populating the dark state and enhancing the EIT resonance amplitude [Fig. 11(b)]. The Zeeman coherence decreases with ellipticity due to a decrease in strength of the σ component but is nonzero for $\varepsilon = 45°$ [Fig. 11(c)].

4. Ellipticity dependence of the EIA and EIT resonance amplitudes

We now consider the variation of the EIA and EIT resonance amplitudes for both scan configurations when the ellipticity is varied (Figs. 5 and 6). The most striking observation is the probe power-dependent peak observed in the EIA amplitude for nonzero ellipticities for longitudinal field scan. Brazhnikov *et al.* [12] first reported this peak and suggested that the peak is due to the Doppler frequency shift for atoms in a gas. One photon detuning due to different velocity groups of atoms made the Hanle profile asymmetric [27]. The EIA amplitude peak was attributed to the result of averaging all such asymmetric profiles with Maxwell-Boltzmann distribution. For longitudinal fields, asymmetric Hanle profiles are also obtained for an EIT resonance. However, no amplitude peak is observed and the resonance amplitude is maximum for $\varepsilon = 0$.

Therefore the factors that influence the amplitude peak require a closer look.

We first note that Hanle EIA profiles computed with a transverse magnetic field for $F_g = 1 \rightarrow F_e = 2$ were found to be symmetric for all ellipticities in the presence of one-photon detuning [Fig. 12(b)]. Asymmetric Hanle profiles obtained at nonzero ellipticities with a longitudinal field scan are also shown for comparison for $F_g = 1 \rightarrow F_e = 2$ [Fig. 12(a)]. Thus we do not expect a peak in resonance amplitude for a transverse field scan at $\varepsilon \neq 0$. This is indeed seen by experiment [Fig. 6(a)], and the computed EIA amplitude variation was found to match well with experimental data [Fig. 13(a)]. Doppler averaging has little influence on the amplitude dependence of the ellipticity. In contrast, Doppler averaging is essential to produce a peak in the computed EIA at intermediate Rabi frequencies for a longitudinal field scan as shown in Fig. 13(b) in good agreement with experiment [Fig. 5(a)].

As noted above the Hanle profiles for $F_g = 1 \rightarrow F_e = 0$ also asymmetric for $\varepsilon \neq 0$ in a longitudinal field scan [Fig. 12(c)] but the EIT amplitude does not exhibit a peak [Fig. 5(b)]. Its ellipticity variation is reproduced well by computation with or without Doppler averaging [Fig. 14(a)]. Results for a transverse field scan computed with and without
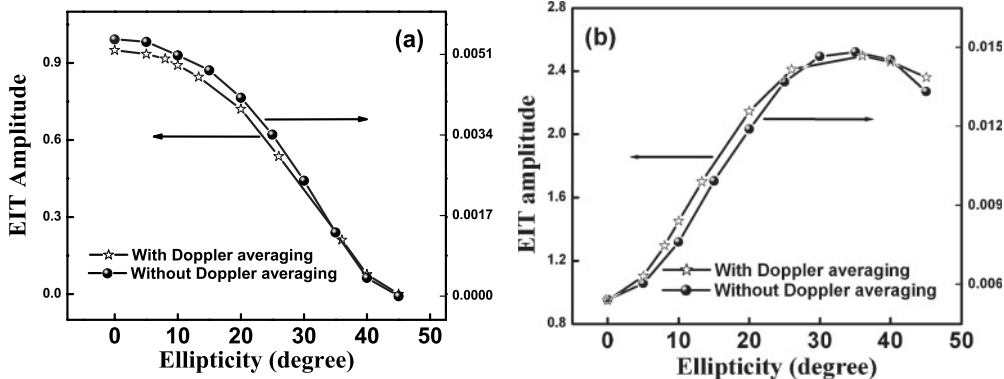

FIG. 14. Computed EIT amplitude for $F_g = 1 \rightarrow F_e = 0$ with a (a) longitudinal field scan and (b) transverse field scan with and without Doppler averaging. Parameters used in computation $\Gamma/\gamma = 1000$, $\Omega/\Gamma = 0.2$, and $b_0 = 1$.
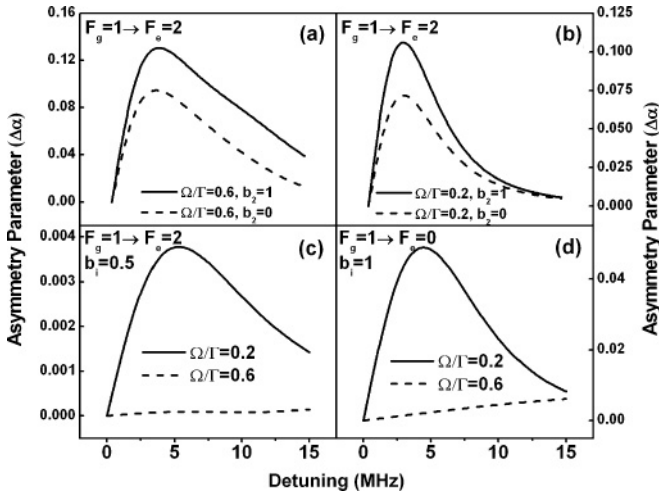
FIG. 15. Computed asymmetry parameter ($\Delta\alpha$) as a function of detuning for $F_g = 1 \rightarrow F_e = 2$ closed system with (a) $\Omega/\Gamma = 0.6$, (b) $\Omega/\Gamma = 0.2$, (c) $F_g = 1 \rightarrow F_e = 2$ open system ($b_i = 0.5$), (d) $F_g = 1 \rightarrow F_e = 0$ closed system with a longitudinal field with $\Gamma/\gamma = 1000$. The Rabi frequencies used are indicated in the plots.

Doppler averaging [Fig. 14(b)] also agree well with experiment [Fig. 6(b)].

In order to understand the factors that influence the ellipticity dependence of the EIA amplitude we define an asymmetry parameter, $\Delta\alpha = \alpha(\omega_L) - \alpha(-\omega_L)$, which represents the difference in absorption at longitudinal magnetic fields, ω_L and $-\omega_L$, all other parameters being the same. From Fig. 12 it can be seen that $\Delta\alpha = 0$ for $\varepsilon = 0$, irrespective of detuning and for $\varepsilon \neq 0$ with zero detuning. For $\varepsilon \neq 0$ and nonzero detuning (1.28 MHz per atomic velocity of 1 m/s), we use $\Delta\alpha$ to represent the asymmetry in the Hanle profile. In Fig. 15 $\Delta\alpha$ is plotted as a function of detuning for the closed transitions, $F_g = 1 \rightarrow F_e = 2$ and $F_g = 1 \rightarrow F_e = 0$, with $\varepsilon = 22.5°$. For $F_g = 1 \rightarrow F_e = 2$ closed transition, increase in Rabi frequency increases the line shape asymmetry at higher detuning [Figs. 15(a) and 15(b)]. However, for $F_g = 1 \rightarrow$

$F_e = 0$, $\Delta\alpha$ is lower and rapidly decreases with increase in Rabi frequency [Fig. 15(d)]. When the TOC from $\Delta m = \pm 2$ coherences is removed ($b_2 = 0$) there is only a marginal decrease in asymmetry [Figs. 15(a) and 15(b)]. Although the Hanle profile exhibits an EIT [Fig. 8, column i, panel (f)], with $b_2 = 0$, the EIA amplitude still exhibits a peak for $\varepsilon \neq 0$ [Fig. 16(a)]. When $F_g = 1 \rightarrow F_e = 2$ is made open by lowering the branching ratio ($b_i = 0.5$), an EIA of lower magnitude is observed [inset of Fig. 16(b)] with significantly lower $\Delta\alpha$ at higher Rabi frequencies [Fig. 15(c)] resembling the behavior observed for $F_g = 1 \rightarrow F_e = 0$ [Fig. 15(d)]. The EIA amplitude computed with (and without) Doppler averaging is a maximum for $\varepsilon = 0$ and no peak is observed for $\varepsilon \neq 0$ [Fig. 16(b)] resembling an EIT resonance for a longitudinal field scan.

The following inferences can be made from these results. The EIA amplitude peak and its shift to higher ellipticities with increase in Rabi frequency stems from the distribution of asymmetry in the Hanle profile with respect to atomic velocities and its dependence on Rabi frequency. Although the off-diagonal terms in the repopulation matrix (coefficients of b_2 in the present case) play a crucial role in the creation of EIA, its influence on $\Delta\alpha$ is minimal and therefore does not influence the EIA amplitude peak. The off-diagonal terms also have a minimal influence on the steady-state population in the excited state.

On the other hand, when the transition is open, the diagonal terms of the repopulation matrix, the excited-state population and excited-state coherences are significantly smaller [28]. As a result, although an EIA is still observed for high Rabi frequencies [28], the distribution of $\Delta\alpha$ with detuning is similar to that observed for a transition exhibiting EIT [Fig. 15(d)] and no amplitude peak is observed. Thus the excited-state population plays a key role in determining the ellipticity dependence of the EIA amplitude. We predict that the amplitude peak will be absent for an open EIA system [29].

In summary EIA and EIT resonances in Hanle geometry were studied experimentally and computationally in longitudinal and transverse magnetic field configurations as function of probe field ellipticity. The EIT resonance observed on
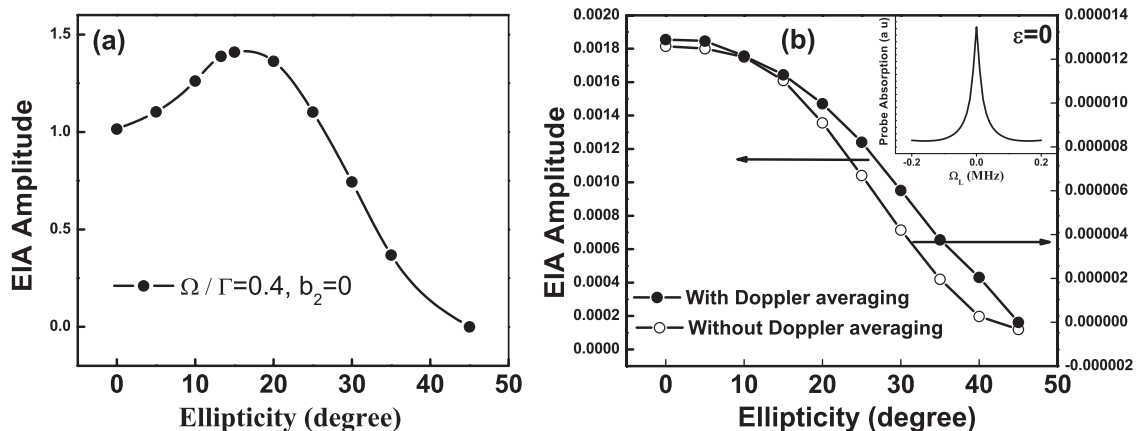

FIG. 16. Computed EIA amplitude for $F_g = 1 \rightarrow F_e = 2$ with a (a) longitudinal field scan with Doppler averaging with $b_0 = 1$, $b_1 = 1$, and $b_2 = 0$ (b) with and without Doppler averaging with $b_0 = 0.5$, $b_1 = 1$, and $b_2 = 1$; inset shows EIA for $\varepsilon = 0$. Parameter used in computation $\Gamma/\gamma = 1000$, $\Omega/\Gamma = 0.4$.

the $F_g = 1 \rightarrow F_e = 2$ transition of ^{87}Rb is a result of the strong influence of the nearby $F_g = 1 \rightarrow F_e = 0$ and $F_g = 1 \rightarrow F_e = 1$ transitions. The decrease and increase in EIA resonance amplitude for longitudinal and transverse magnetic fields respectively were accounted for in terms of the transfer of Zeeman coherences from the excited state to the ground state. It was shown that the ellipticity dependence of the EIA amplitude for a transverse field scan can be accounted for without invoking the Doppler effect unlike a longitudinal field scan. The EIA amplitude peak observed for nonzero ellipticities was found to strongly depend on the closedness of the transition and therefore the steady-state excited-state population. We predict that the ellipticity dependence of the EIA amplitude for an open system should not exhibit a peak in a longitudinal magnetic field and resemble the behavior observed in EIT systems.

[1] M. Fleischhauer, A. Imamoglu, and J. P. Marangos, Rev. Mod. Phys. **77**, 633 (2005).

[2] A. M. Akulshin, S. Barreiro, and A. Lezama, Phys. Rev. A **57**, 2996 (1998).

[3] H. R. Gray, R. M. Whitley, and C. R. Stroud, Opt. Lett. **3**, 218 (1978).

[4] M. O. Scully, S. Y. Zhu, and A. Gavrielides, Phys. Rev. Lett. **62**, 2813 (1989).

[5] A. Kasapi, M. Jain, G. Y. Yin, and H. E. Harris, Phys. Rev. Lett. **74**, 2447 (1995).

[6] M. Hashimoto and M. Ohtsu, IEEE J. Quantum Electron. **23**, 446 (1987).

[7] D. Budker, D. F. Kimball, S. M. Rochester, V. V. Yashchuk, and M. Zolotorev, Phys. Rev. A **62**, 043403 (2000).

[8] A. Lezama, S. Barreiro, and A. M. Akulshin, Phys. Rev. A **59**, 4732 (1999).

[9] A. V. Taichenachev, A. M. Tumaikin, and V. I. Yudin, Phys. Rev. A **61**, 011802 (1999).

[10] H. Failache, P. Valente, G. Ban, V. Lorent, and A. Lezama, Phys. Rev. A **67**, 043810 (2003).

[11] Y. Dancheva, G. Alzetta, S. Cartaleva, M. Taslakov, and C. Andreeva, Opt. Commun. **178**, 103 (2000).

[12] D. V. Brazhnikov, A. V. Taichenachev, A. M. Tumaikin, V. I. Yudin, S. A. Zibrov, Y. O. Dudin, V. V. Vasil'ev, and V. L. Velichansky, JETP Lett. **83**, 64 (2006).

[13] J. Dimitrijevic, Z. Grujic, M. Mijailovic, D. Arsenovic, B. Panic, and B. M. Jelenkovic, Acta Phys. Pol. A **112**, 841 (2007).

[14] J. Dimitrijevic, Z. Grujic, M. Mijailovic, D. Arsenovic, B. Panic, and B. M. Jelenkovic, Opt. Express **16**, 1343 (2008); A. J. Krmpot, M. Mijailovic, B. Panic, D. V. Lukik, A. G. Kovacevic, D. V. Pantelic, and B. M. Jelenkovic, *ibid.* **13**, 1448 (2005).

[15] J. Dimitrijevic, D. Arsenovic, and B. M. Jelenkovic, Phys. Rev. A **76**, 013836 (2007).

[16] F. Renzoni, S. Cartaleva, G. Alzetta, and E. Arimondo, Phys. Rev. A **63**, 065401 (2001).

[17] C. Andreeva, A. Atvars, M. Auzinsh, K. Blush, S. Cartaleva, L. Petrov, and D. Slavov, Phys. Rev. A **76**, 063804 (2007).

[18] M. Auzinsh, R. Ferber, F. Gahbauer, A. Jarmola, and L. Kalvans, Phys. Rev. A **79**, 053404 (2009).

[19] A. S. Zibrov and A. B. Matsko, JETP Lett. **82**, 472 (2005).

[20] G. Alzetta, S. Cartaleva, Y. Dancheva, C. Andreeva, S. Gozzini, L. Botti, and A. Rossi, J. Opt. B:Quantum Semiclass. Opt. **3**, 181 (2001).

[21] M. O. Scully and M. S. Zubairy, *Quantum Optics* (Cambridge University Press, New York, 1997).

[22] Computed with a user-extensible Mathematica based atomic density matrix package, ATOMICDENSITYMATRIX, Simon Rochester. Available online at [http://budker.berkeley.edu/ADM]. A detailed account of the theoretical framework can be found at: Yu. P. Malakyan, S. M. Rochester, D. Budker, D. F. Kimball, and V. F. Yashchuk, Phys. Rev. A **69**, 013817 (2004).

[23] N. Ram, J. Anupriya, M. Pattabiraman, and C. Vijayan, J. Phys. B: At. Mol. Opt. Phys. **42**, 175504 (2009).

[24] F. Renzoni, C. Zimmermann, P. Verkerk, and E. Arimondo, J. Opt. B: Quantum Semiclass. Opt. **3**, S7 (2001).

[25] T. Zigdon, A. D. Wilson-Gordon, and H. Friedmann, Phys. Rev. A **77**, 033836 (2008).

[26] D. Budker, D. F. Kimball, and D. P. DeMille, *Atomic Physics* (Oxford University Press, London, 2004).

[27] D. V. Brazhnikov, A. M. Tumaikin, V. I. Yudin, and A. V. Taichenachev, J. Opt. Soc. Am. B **22**, 57 (2005).

[28] C. Goren, A. D. Wilson-Gordon, M. Rosenbluh, and H. Friedmann, Phys. Rev. A **67**, 033807 (2003).

[29] EIA resonances were observed with respect to pump-probe detuning in $F_g = 2 \rightarrow F_e = 3$ ($D1$; ^{85}Rb) and $F_g = 1 \rightarrow F_e = 2$ ($D1$; ^{87}Rb) by Kim *et al.*: S. K. Kim, C. H. Lee, K. Kim, J. B. Kim, and H. S. Moon, J. Korean Phys. Soc. **42**, 488 (2003).